

Rings and Jets around PSR J2021+3651: the ‘Dragonfly Nebula’

Adam Van Etten¹, Roger W. Romani¹ & C.-Y. Ng²

ave@stanford.edu, rwr@astro.stanford.edu, ncy@physics.usyd.edu.au

ABSTRACT

We describe recent Chandra ACIS observations of the Vela-like pulsar PSR J2021+3651 and its pulsar wind nebula (PWN). This ‘Dragonfly Nebula’ displays an axisymmetric morphology, with bright inner jets, a double-ridged inner nebula, and a $\sim 30''$ polar jet. The PWN is embedded in faint diffuse emission: a bow shock-like structure with standoff $\sim 1'$ brackets the pulsar to the east and emission trails off westward for 3-4'. Thermal ($kT_\infty = 0.16 \pm 0.02$ keV) and power law emission are detected from the pulsar. The nebular X-rays show spectral steepening from $\Gamma = 1.5$ in the equatorial torus to $\Gamma = 1.9$ in the outer nebula, suggesting synchrotron burn-off. A fit to the ‘Dragonfly’ structure suggests a large ($86 \pm 1^\circ$) inclination with a double equatorial torus. Vela is currently the only other PWN showing such double structure. The >12 kpc distance implied by the pulsar dispersion measure is not supported by the X-ray data; spectral, scale and efficiency arguments suggest a more modest 3-4 kpc.

Subject headings: pulsars: individual (PSR J2021+3651) — stars: neutron — gamma-rays — observations

1. Introduction

Pulsars inject a relativistic particle wind into their surroundings, tapping their rotational kinetic energy. This energetic wind is concentrated toward the spin equator and, shocking against the surrounding medium, causes particle acceleration and pitch angle scattering that results in a synchrotron nebula (Rees & Gunn 1974; Kennel & Coroniti 1984). Approximately 50 pulsars have an associated PWN, and the polar jet/equatorial torus morphology is now seen to be quite common (Kargaltsev & Pavlov 2008). Many of the mechanisms governing the energetics and evolution of pulsar/PWN systems are still unknown, such as how

¹Department of Physics, Stanford University, Stanford, CA 94305

²School of Physics, University of Sydney, NSW 2006, Australia

rotational kinetic energy is converted to particle outflow, the manner in which polar jets are confined, and the details of charge acceleration. The structure of PWNe offer insights into these puzzles, and also probe pulsar geometry, relativistic shocks, and the properties of the ambient medium. PSR J2021+3651 (hereafter J2021) is interesting for its highly structured PWN, and is also a likely counterpart of the EGRET gamma ray source GEV 2020+3658. Pulsars detected in GeV gamma rays are currently of great interest with the successful launch of AGILE and the imminent launch of GLAST.

Timing observations of this 103.7 ms pulsar show that J2021 is young and energetic [characteristic age $\tau_c = P/(2\dot{P}) = 1.7 \times 10^4$ yr and spindown luminosity $\dot{E} = 4\pi^2 I \dot{P} P^{-3} = 3.4 \times 10^{36}$ ergs s $^{-1}$], despite being rather radio faint with a 1.4 GHz flux density $S_{1400} \approx 0.1$ mJy (Roberts et al. 2002; Hessels et al. 2004). The dispersion measure of 369 cm $^{-3}$ pc places it ~ 12 kpc away on the far edge of the outer spiral arm, according to the NE2001 electron model of the galaxy (Cordes & Lazio 2002). Although its spin characteristics are similar to those of other γ -ray pulsars [Vela: $d \approx 300$ pc (Dodson et al. 2003), $P = 89.3$ ms, $\dot{E} = 6.9 \times 10^{36}$ ergs s $^{-1}$; B1706–44: $d \sim 3$ kpc (Romani et al. 2005), $P = 103$ ms, $\dot{E} = 3.4 \times 10^{36}$ ergs s $^{-1}$], the 12 kpc distance assumed from the dispersion measure would make it extraordinarily γ -ray efficient, as discussed by Roberts et al. (2002).

Roberts, Romani, & Kawai (2001) noted the possible connection between GEV J2020+3658 and ASCA source AX J2021.1+3651. The ASCA data revealed spatially unresolved emission extending $\sim 8'$ east to west and $\sim 4'$ north to south, with a hydrogen column density of $N_H = 5.0 \pm 2.5 \times 10^{21}$ cm $^{-2}$, and a power-law spectrum with $\Gamma = 1.73^{+0.26}_{-0.28}$. The following year a targeted radio search by Roberts et al. (2002) discovered J2021; these authors reanalyzed the ASCA data and concluded that a thermal component ($kT \sim 0.1$ keV) in addition to the absorbed power law improved the fit to the data, giving an $N_H = 7.6^{+4.7}_{-3.5} \times 10^{21}$ cm $^{-2}$. Hessels et al. (2004) were able to resolve the inner equatorial PWN and jets surrounding J2021 with a 19 ks *Chandra* ACIS-S observation, noting a toroidal morphology and possible double structure; this observation had a sub-framed field of view and could not probe the faint larger-scale structure. These authors report an N_H of $7.8^{+1.7}_{-1.4} \times 10^{21}$ cm $^{-2}$, a power law index of $\Gamma = 1.73^{+0.3}_{-0.2}$ in the extended emission. Thermal emission from the pulsar at $kT_\infty = 0.15 \pm 0.02$ keV was noted, along with a possible pulse fraction of 65% from the pulsar, presumably mostly due to thermal emission. We describe here a deeper *Chandra* exposure, which better resolves the innermost structure and maps the outer portions of the nebula. The improved constraints on spectral and morphological parameters of the PWN afforded by this deeper observation can help address the question of the pulsar's distance and will be helpful in interpreting future high energy observations.

2. Observations and Data Analysis

We observed J2021 with *CXO* in the ACIS-S configuration (chips 2-3 and 5-8), with the pulsar positioned near the standard aim-point on the S3 chip during two epochs: December 25-26 2006 with a total live time of 33.8 ks (obsID 8502 = ‘obs1’) and December 29-30 2006 for 59.4 ks (obsID 7603 = ‘obs2’). All figures shown below are merged images of the two observations. The CCDs were operated in VFaint mode to improve rejection of particle backgrounds. Neither observation exhibited significant flaring, so we include all the data in the analysis, for a total live time of 93.2 ks. These data are also compared with an archival 19.0 ks observation on chips 6-8 taken on February 12 2003 (obsID 3901 = ‘obs0’). For that exposure, the chips were windowed to 1/4 frame, covering only the bright central region of the PWN, as described in Hessels et al. (2004).

The data were analyzed using CIAO 3.4.0 and CALDB 3.4.0. We started with level=1 event files, removed pixel randomization, applied time-dependent gain and CTI corrections, and implemented a background cleaning algorithm for VFaint mode which uses the outer 16 pixels of the 5×5 event island to improve discrimination between good events and likely cosmic rays. HEASARC’s WebPIMMS tool estimates a small pileup fraction of 1.6% at the pulsar location. Since the pileup is low, we improve the spatial resolution of the ACIS image by applying an algorithm to correct the position of split pixel events Mori et al. (2001); this decreases the on-axis PSF width in our data set by $\sim 13\%$.

In order to determine the background count rate, we located a region of the S3 chip relatively free of diffuse emission, cut out point sources, and measured a count rate of 0.59 counts s^{−1} in the 0.5-7 keV band. Since much of the S3 chip is covered by diffuse nebulae, we split the background region into two parts: the southern corner of the chip, as well as a portion of the chip northwest of the pulsar, exterior to the extended emission. The nominal background count rate for the S3 chip in this band is 0.32 counts s^{−1}. Although no large background flares were seen, solar activity was high during the observations which may contribute to the increased background. It is also likely that low surface-brightness diffuse emission from either extended PWN structure or Galactic background makes a non-negligible contribution.

2.1. X-ray Spatial Analysis

In order to bring out the large scale diffuse emission, we excised point sources (retaining the pulsar and a few other sources of interest), exposure-corrected the image to minimize chip gaps, and smoothed with a 6'' FWHM Gaussian. Figure 1 reveals considerable emission

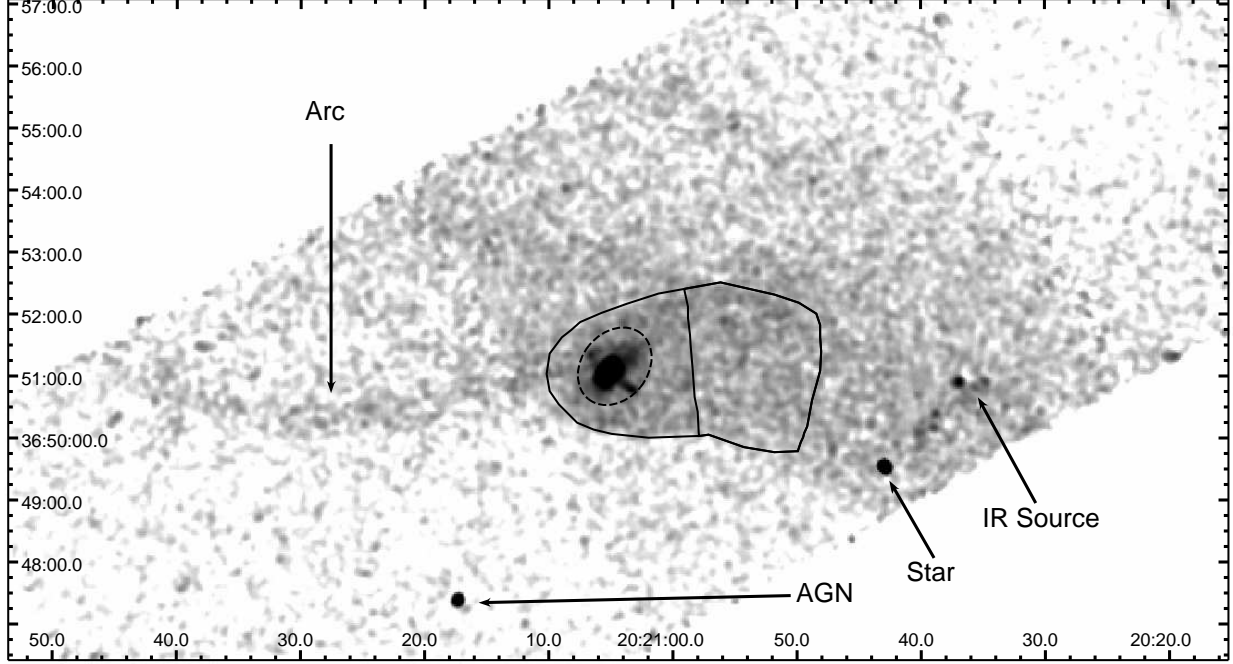


Fig. 1.— ACIS-S 1-7 keV image (exposure corrected, 6'' Gaussian smoothing). Point sources have been removed except for the AGN candidate, a bright USNO star, and four sources coincident with a diffuse IR nebula. Extraction regions for the outer nebula (and dotted exclusion region) are also shown.

surrounding the pulsar located at R.A. = 20:21:05.43, decl. = +36:51:04.63. A thin arc of emission extends 7'.7 east from the pulsar to the edge of the S2 chip. To the west, diffuse emission covers much of the S3 chip and extends onto S4. The southern boundary of this emission is very pronounced, with a sharp arc bracketing the pulsar to the east and south.

The pulsar is surrounded by an axisymmetric inner nebula extending $20'' \times 10''$ with two ridges of emission flanking the pulsar point source. Southwest of the pulsar is a very bright inner jet 4'' long, while to the northeast a similar, albeit dimmer, feature forms an inner counter jet. On larger scales the jet can be followed in a fainter extension from 4'' to 10'', and intensifies to a bright, narrow outer jet running 12'' to 30'' from the pulsar. This outer jet ends in a distinct knot of emission. On the opposite (‘counter-jet’) side the extended jet is not obvious. However, there is a hard, unresolved source 23'' from the pulsar roughly along the counter-jet axis with no obvious stellar counterpart; this is plausibly the counterpart of the jet knot to the south. The emission from the outer jets may be variable. For example Hessels et al. (2004) did not conclusively detect the outer jet. In obs0, the structure is not visually apparent with $9.0 \pm 4.7 \times 10^{-4}$ counts s $^{-1}$ from this region, while in

the new data the outer jet produces a significant detection with $1.3 \pm 0.2 \times 10^{-3}$ counts s $^{-1}$ above a surrounding background annulus. There is also no detection of the jet terminal knot in obs0. In contrast, Hessels et al. (2004) describe a diffuse structure on the counter-jet side. We remeasure this region and find $1.9 \pm 0.5 \times 10^{-3}$ counts s $^{-1}$ in obs0; the same region in the new data contributes $1.0 \pm 0.2 \times 10^{-3}$ counts s $^{-1}$ above the local background. While the excess is formally significant, there is no obvious coherent structure extending to the northern knot. Of course, variation in extended jet structure is not unexpected: the Vela pulsar outer jet displays dramatic variability on timescales of days to weeks (Pavlov et al. 2003).

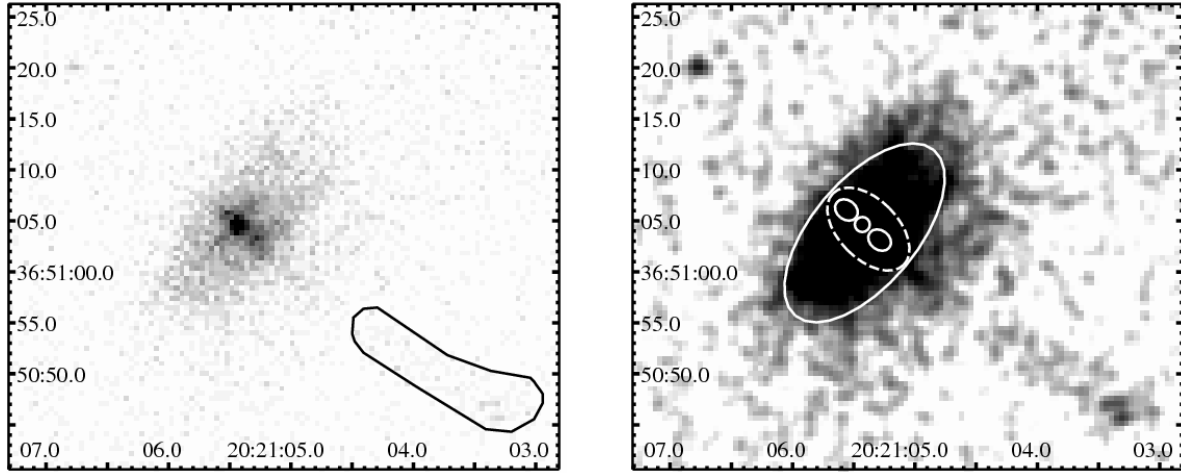


Fig. 2.— 1-7 keV images. Left: A soft stretch shows the double ‘ridge’ structure of the equatorial PWN, along with the extraction aperture of the outer jet. Right: A deeper stretch and 1'' Gaussian smoothing bring out the diffuse emission and jets. The extraction apertures for the pulsar, inner jets and equatorial PWN (with dashed exclusion region) are shown against the PWN.

Turning to the central, brightest portion of the PWN, we see two ridges of X-ray emission perpendicular to the jet symmetry axis, one crossing just above the pulsar position and one crossing the bright inner jet. As noted in Hessels et al. (2004), this suggests a double torus structure, like that of Vela, but seen more nearly edge-on. We further explore the PWN structure by fitting torus models in §2.2 below. There is a tradition of naming PWNe after animals, dating back to the fancied resemblance of the remnant of SN1054 in a drawing from visual observations by William Parsons, Earl of Rosse (1844) to, variously, a crab or a crab’s claw. For the J2021 PWN, we have a double ridge extending to each side of the pulsar and a single bright narrow jet. We thus christen this the ‘Dragonfly Nebula’ with the double ridge forming the paired wings and the outer jet forming the tail.

As usual in any deep Galactic exposure, several dozen unresolved sources, many coincident with field stars, are detected in our image. We mention here only the sources of particular interest. One of the brightest sources in the field, CXOU J202117.4+364723.7, has a hard, absorbed spectrum and no optical, IR, or radio counterpart. We consider this a likely AGN viewed through the plane. Roughly $4'.7$ southwest of the pulsar, a strong X-ray source is seen coincident with the bright field star USNO-B1.0 1268-00448692.

Examination of MSX $8\mu\text{m}$ data shows a cavity coincident with the X-ray nebula. In particular, the southern edge of the nebula coincides with a fairly sharp step in the $8\mu\text{m}$ flux (Figure 3). This can be interpreted as a dust deficit in the X-ray nebula interior, caused by evaporation of embedded dust grains. The trail also seems to correlate with a faint 1.4GHz continuum in the DRAO GPS maps, but more sensitive imaging would be needed to confirm the reality of this structure. At the west end of this cavity the MSX $8\mu\text{m}$ data shows a peculiar double-lobed diffuse ($1'.7 \times 2'$) object, centered at 20:20:36.1 +36:50:37 (Figure 3). The center of this object is within $40''$ of the $S_{1.4\text{GHz}} = 25.8 \pm 4.1$ mJy source NVSS J202036+365123. Intriguingly Pavlov et al. (2007) noted a double-lobed mid-IR/radio nebula of similar size near PSR B1823–13 and its PWN, although the pulsar proper motion argues against association in this case. Four of the faint X-ray sources are coincident with the IR nebula. Three of the X-ray sources lie within the lobes, while the fourth is in the bisecting dark lane. All appear absorbed with virtually no counts below 1 keV; the association with the IR complex, if any, is not obvious.

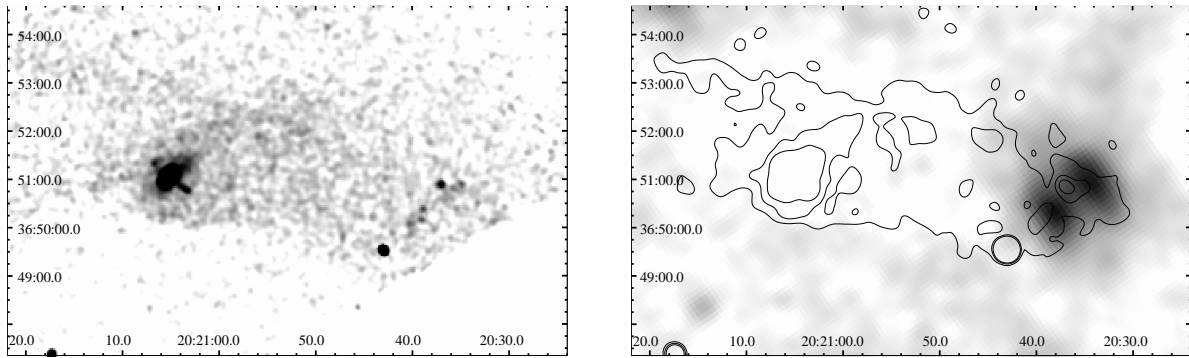


Fig. 3.— Left: ACIS image with $3''$ Gaussian smoothing showing the PWN, jets, and outer nebula trailing off to the west. Right: MSX A-band image ($8.3\mu\text{m}$) overlaid with heavily smoothed contours from the X-ray data – a $8.3\mu\text{m}$ deficit follows the outer PWN; faint X-ray point sources are found in the bright double-lobed IR source.

2.2. Spatial Modeling of the Inner Nebula

In the introduction we noted that many PWNe display axisymmetric torus and jet structures formed from a relativistic wind with significant latitudinal variation. MHD simulations of such winds (Komissarov & Lyubarsky 2004; Del Zanna et al. 2006; Bucciantini 2007) show that Doppler boosted arcs and jets can appear in synchrotron emissivity maps, often associated with lines-of-sight tangential to discontinuities in the flow. For the brightest PWNe (i.e. Crab and Vela) the *CXO* images are sufficiently detailed for comparison with these models. For more typical sources, only the overall scale, orientation and Doppler enhancement can be measured. These parameters can be useful for probing several aspects of pulsar physics (Ng & Romani 2008). Even when the PWN structures are less than visually stunning, Ng & Romani (2004) showed that it is possible to extract robust values for the basic angles and scales by fitting a simplified Doppler boosted torus model to the *CXO* images. Following their methodology, we fitted the ‘Dragonfly Nebula’ with a double torus model similar to that of the Vela PWN, including a point source and a uniform background. The fitting minimizes residuals using a Poisson-based likelihood function. We estimated the statistical errors by re-fitting Monte Carlo simulations of the best-fit model. The systematic errors are estimated by in turn re-fitting the data with the jets and point source regions removed; see Ng & Romani (2008) for details.

For comparison, we also tried fitting with a single torus model; in this case, a large torus thickness, or ‘blur’, is required for a viable fit. This single torus model does a substantially poorer job of matching the inner structure near the pulsar. For example, if we exclude the pulsar and jets and collapse the counts along the symmetry axis there is a clear dip between the tori in the nebula brightness profile, 0.5–2′.5 SW of the pulsar. In this region the single torus model departs from the data at the 6σ level. However the large ‘blur’ in the single torus model allows it to fit the general excess of diffuse emission skirting the PWN better than the sharper two-torus model (see Figure 4). This allows the fit statistic to be of comparable quality. Thus with a free fit, the double torus model is preferred, but not definitively so. If an extra ‘halo’ component were added to the model, the preference for the double torus would be stronger, but this is not really required by the present data quality.

Figure 4 shows the data in 0.5–8 keV band compared to the best-fit models, with the parameters listed in Table 1: the axis position angle Ψ , inclination angle ζ , torus radius R , blur δ for the torus profile, post-shock flow velocity β , and separation d . The best-fit orientation parameters are consistent in both models, though R changes slightly due to the different blur. The new results also show good agreement with the previous fits by Hessels et al. (2004), but provide more precise measurements. The relatively small errors indicate that the fits are robust and not sensitive to the presence of the jets. In summary,

the numerical fits confirm our visual impression that the double structure better matches the data. However, unless we allow extra model components to absorb the extended halo counts or fix the blur δ at small values for both models, the fit statistic for the single torus is not dramatically worse. Note that the Poisson statistics employed here preclude a direct comparison of the two models with the F -test.

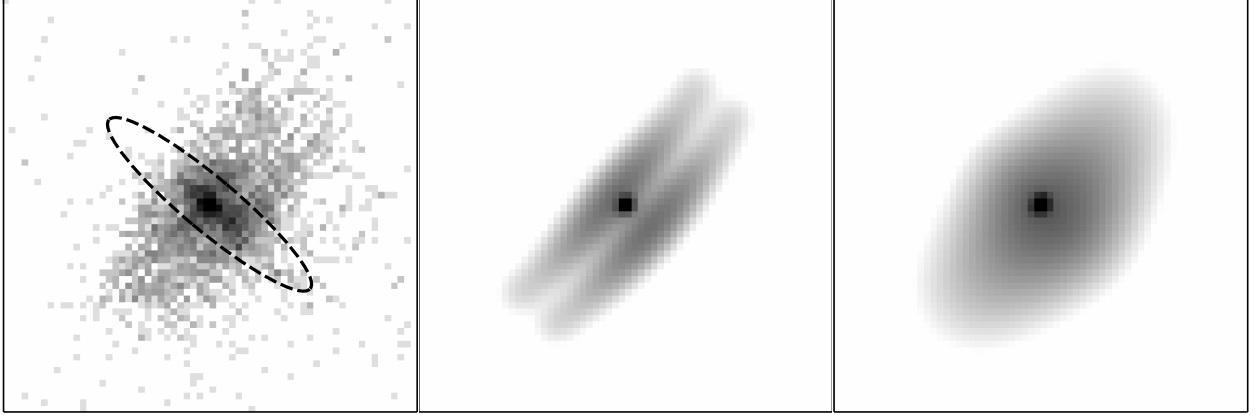


Fig. 4.— 0.5-8 keV image compared to the best-fit double tori and single torus models. The dotted ellipse shows the region excised to estimate systematic errors.

2.3. Spectral Analysis

We used CIAO’s Sherpa environment (version 3.4) and XSPEC (version 12.3.1) to fit the spectra of the pulsar and nebula. For consistency, we bin all spectra to a signal-to-noise ratio of three; as a result the jet was fit only with the new data sets, as the old observation (obs0) has insufficient counts. The extended emission lies outside the field of view of obs0, and therefore must also be fit with the new data sets alone. Careful background subtraction is important for robust spectral fitting; for the inner jets we subtract the surrounding inner nebula as background, for the star and AGN we utilized surrounding annuli, and for all other regions we used a large source-free background region. This background region is on the S3 chip for all spectral fits except for the eastern wisp, which uses a background region on the S2 chip. Fit errors are projected multi-dimensional values at the 90% confidence level, except for fluxes. Multi-dimensional flux error estimates are often quite large due to spectral parameter uncertainties, so we list single parameter errors at the 90% confidence level.

We determined the interstellar absorption for the pulsar/PWN complex by simultaneously fitting the inner and outer components of the nebula with a global N_{H} , but different power-laws; this yields a hydrogen column density of $6.7^{+0.8}_{-0.7} \times 10^{21} \text{ cm}^{-2}$, consistent (albeit

with much smaller errors) with the Roberts, Romani, & Kawai (2001) value of $5.0 \pm 2.5 \times 10^{21} \text{ cm}^{-2}$, Roberts et al. (2002) value of $N_{\text{H}} = 7.6_{-3.5}^{+4.7} \times 10^{21} \text{ cm}^{-2}$ and the Hessels et al. (2004) value of $7.8_{-1.4}^{+1.7} \times 10^{21} \text{ cm}^{-2}$. The value of $6.7 \times 10^{21} \text{ cm}^{-2}$, is adopted in all final fits to components of the PSR/PWN complex. Although the soft thermal spectrum of the pulsar itself provides many photons, the effective temperature is highly covariant with N_{H} ; accordingly fits to the relatively simple power laws of the extended non-thermal emission provide the best absorption constraints. The two brightest point sources have absorptions bracketing the pulsar value. The field star B1.0 1268-00448692 gave a low N_{H} of $0.2 \times 10^{21} \text{ cm}^{-2}$. A power-law fit to our candidate AGN gives $N_{\text{H}} = 2.2 \times 10^{22} \text{ cm}^{-2}$, $\sim 3 \times$ larger than the PSR/PWN value. This supports its identification as an extragalactic source, although some of the absorption may be intrinsic.

2.3.1. Pulsar Spectrum

To measure the spectrum of the point source with minimal nebular contamination, we define a source region of radius 1.5 pixels ($0''.74$). Pulsar spectral fitting is complicated by the fact that the inner nebula surface brightness scales inversely with radius; extrapolating the radial profile indicates that the nebular surface brightness is $\sim 2.5 \times$ greater in the source region than in an annulus extending 2.5 to 6 pixels radially from the pulsar. This precludes simple annular background subtraction. Instead we determine the nebular power law in this surrounding annulus and scale up the amplitude as predicted from the brightness profile, giving an unabsorbed 0.5-8 keV flux of $4.1 \times 10^{-14} \text{ erg/cm}^2/\text{s}$ and $\Gamma=1.20$. We hold this amplitude and Γ fixed as a contribution to the background in the pulsar aperture, while fitting the pulsar point source spectral model. Both the pulsar and annulus regions utilized the large source-free background region on the S3 chip.

For point source fluxing, we modeled the necessary aperture correction by simulating 10 monochromatic PSFs from 0.5 to 9.5 keV with the Chandra Ray-Trace program, ChaRT. The enclosed energy fraction as a function of radius was then calculated to correct the ARFs used in the spectral fit. We fit four different models: a blackbody (BB), a power law plus blackbody (PL+BB), a magnetized neutron star hydrogen atmosphere (NSA), and a power law plus neutron star atmosphere (PL+NSA) (Zavlin et al. 1996), all with the extra fixed power law component from the nebular background. As a check, we also fit allowing N_{H} to vary. The fitted model parameters were consistent with those found using the N_{H} fixed by the nebula fits, albeit with increased errors. For multi-component models, covariance between components will induce larger effective flux errors – e.g. for the power law plus atmosphere model the power law component flux errors increase from $\sim 22\%$ to

$\sim 26\%$ allowing for component covariance (spectral parameters fixed). The errors grow to $\sim 100\%$ if all spectral parameters are free.

Adding a second thermal component to the simple blackbody model improves the fit, but since the pulsar has significant counts above 3keV, a high temperature $T_2 \sim 1.5\text{keV}$ and small area $A_2 \sim 10^{-5}A_1$ would be required. A similar result is achieved for a two temperature neutron star atmosphere fit. The small area of the secondary component does not seem compatible with a polar cap for a Vela-type pulsar. The power law plus blackbody and power law plus neutron star atmosphere models also yield much better fits than the simple absorbed blackbody or NSA models. This point source non-thermal PL component may represent either magnetospheric emission or unresolved PWN structure. We favor the former, since the component contributes more flux than the nebular extrapolation. Although the nebular extrapolation is uncertain, varying over a plausible range only induced $\sim 10\%$ changes in the point source PL flux.

Our PL+BB model returns a kT_∞ of $0.16 \pm 0.02\text{ keV}$ which matches well to the Hessels et al. (2004) fit of $0.15 \pm 0.02\text{ keV}$. This value is also comparable to that of the similarly-aged Vela pulsar ($\tau_c = 11\text{ kyr}$, $kT_\infty = 0.128 \pm 0.003\text{ keV}$, Pavlov et al. 2001) and B1706–44 ($\tau_c = 17\text{ kyr}$, $kT_\infty = 0.17 \pm 0.02\text{ keV}$, Romani et al. 2005). The thermal fits allow us to calculate an effective radius as a function of distance, and hence the emitting area. For the moment we set the scale with a nominal distance of 10 kpc (so $d = 10d_{10}\text{ kpc}$), although as we see below smaller distances are preferred. Our fit to a power law plus blackbody with N_H fixed gives $R = 7.0^{+4.0}_{-1.7}d_{10}\text{ km}$, representing emission from $29^{+42}_{-12}\%$ of the stellar surface for a $R_\infty = 13.1\text{ km}$ star. The minimum emitting area of $8.8 \times 10^{11}d_{10}^2\text{ cm}^2$ is far greater than that of the traditional polar cap $A_{pc} = 2\pi^2 R^3/cP \approx 6.3 \times 10^9\text{ cm}^2$ for any reasonable distance.

Blackbody deviations for NSA models in principle allow one to determine both radius and surface redshift, although in CCD quality data these are highly degenerate. Consequently, in fitting model atmospheres we fix the surface radius at $R_s = 10\text{ km}$, corresponding to $R_\infty = R_s(1 - 2GM/R_sc^2)^{-1/2} = 13.1\text{ km}$. The neutron star mass is fixed at $M = 1.4\text{ M}_\odot$, and we use models with a surface magnetic field of 10^{12}G . With the mass and radius fixed, the pulsar distance is determined directly from the model normalization. With N_H fixed our NSA+PL fit yields a distance of $2.1^{+2.1}_{-1.0}\text{ kpc}$, where the distance error includes multi-parameter uncertainty. As usual the NSA model’s Wien excess requires a lower T_{eff} and a smaller distance than that found from blackbody model fits. For a similar NSA+PL fit Pavlov et al. (2001) report a T_∞ of 0.059 keV from Chandra ACIS-S observations of the Vela pulsar. These authors infer a distance of $220 \pm 20\text{ pc}$ from their neutron star normalization, which is within 25% of the accepted $\sim 300\text{ pc}$ distance. Our J2021 neutron star atmosphere normalization distance estimate of 2.1 kpc therefore lends some credence to the assertion

that the pulsar is significantly closer than 12 kpc.

2.3.2. *Extended Source Spectra*

As a check, we fit the spectra for the inner and outer nebulae independently, allowing N_H to vary; we find $N_H = 6.7^{+1.1}_{-1.0} \times 10^{21} \text{ cm}^{-2}$ and $N_H = 6.6^{+1.1}_{-1.0} \times 10^{21} \text{ cm}^{-2}$ respectively, fully consistent with the global absorption fit above. Using the fixed global N_H allows us to extract useful spectral index estimates for various components of the PWN complex. The large arc east of the pulsar may or may not be associated with J2021. Accordingly we also fit this spectrum allowing N_H to vary, though with the larger errors the result is not very constraining.

As one moves progressively further from the pulsar the extended emission exhibits significant softening, as expected from synchrotron burn-off in the outer PWN. The inner jets have the hardest spectra ($\Gamma=1.1$), while the outer jet region is softer with $\Gamma=1.7$. The inner nebula or ‘equatorial PWN,’ has $\Gamma = 1.5$. The diffuse trail close to the pulsar ($\approx 30''$ - $60''$) has a power-law index of 1.7, while in the farther reaches of the outer nebula we observe an index of 1.9.

2.3.3. *USNO Star Spectrum*

We estimated a photometric parallax for USNO-B1.0 1268-00448692 using data from the USNO-B ($\sim B, R, I$ bands) and 2MASS catalogs (J, H, K_s bands). We converted the survey magnitudes to standard colors and fit the colors to stellar values (Kenyon & Hartmann 1995) subject to interstellar reddening (Schlegel et al. 1998). The best global fit to main sequence colors implied class M2 V, with $A_V \approx 0.45$ at a distance of ~ 60 pc. The POSS-II ‘I’ band point has the largest departure from the model colors; if it is excluded the best class shifts to K6 V with $A_V \approx 1.7$ at ~ 100 pc. Few post-MS stars of this color emit coronal X-rays. The best match (excluding I) was a rather implausible G5 III with $A_V \approx 2.7$ at 1.5 kpc.

The star shows modest variability within and between epochs. We therefore follow the procedure of Getman et al. (2005) and adopt a two component Mekal plasma model; we fit the temperatures and amplitudes separately for each observation, while fitting for a common $N_H = 0.2 \times 10^{21} \text{ cm}^{-2}$. As expected the star temperatures are higher during the X-ray bright epochs. The fit N_H can be compared with the optical extinction, where $N_H = A_V 1.9 \times 10^{21} \text{ cm}^{-2}$ predicts $A_V = 0.4^{+0.2}_{-0.4}$. The best global interpretation thus appears to be a relatively mundane nearby M2 V field star; the estimated N_H and A_V are in reasonable

agreement, albeit somewhat higher than one would expect for a 60 pc distance. However this extinction adds no significant contribution to the full column to J2021.

3. Discussion

3.1. Distance

As noted in the introduction, the dispersion measure of $369 \text{ cm}^{-3} \text{ pc}$ ($N_e = 1.13 \times 10^{21} \text{ cm}^{-2}$) for J2021 corresponds to a distance of 12 kpc in the Cordes & Lazio (2002) model. Such a large distance is problematic on several grounds, so it is important to check this estimate against other observables. Our best fit hydrogen column density is $N_H = 6.7 \times 10^{21} \text{ cm}^{-2}$, while the total Galactic N_H in the direction of J2021 is estimated from HI maps to be $1.2 \times 10^{22} \text{ cm}^{-2}$ according to Dickey & Lockman (1990) or $9.7 \times 10^{21} \text{ cm}^{-2}$ according to Kalberla et al. (2005). Thus we already detect somewhat less than the expected column, suggesting that J2021 does not reside in the far reaches of the Galaxy. Moreover, with $N_H = 2.2 \pm 0.9 \times 10^{22} \text{ cm}^{-2}$ measured for our AGN candidate an even higher column is implicated (although, again, some of this absorption may be intrinsic). On the balance, these data suggest that the pulsar/PWN absorption, while large, is $\sim 1/3 - 2/3$ the full Galactic column density in this direction, placing the source well inside the Milky way disk.

According to Cordes & Lazio (2002), DM distance estimates are seldom off by $> 50\%$, unless the line of sight intersects anomalously dense electron clouds. In any case, at such large DM it is difficult for any one HII region to substantially increase the value. Nevertheless, we note that our observed neutral to ionized ratio $N_H/N_e \approx 6$ is somewhat below the canonical factor of 10, while Hessels et al. (2004) noted that J2021’s radio pulse profile showed anomalous scattering with a scattering measure $SM \sim 100\times$ that predicted by the NE2001 model. These provide evidence for high ionization along the line of sight. However, none of the X-ray structures that we see provide an obvious source of such ionized gas: the ‘Arc’ passes north of the pulsar and the extended nebula is too faint to represent a large emission measure or column density.

One problem with the large 12 kpc distance would be the high γ -ray efficiency. For an assumed 1sr beaming, the observed 3EG point source γ -ray flux gives a 0.1-5 GeV efficiency of $\eta_\gamma \equiv L_\gamma/\dot{E} \sim 0.15 d_{10}^2$. We should compare this with the similar γ -ray pulsars Vela ($d \approx 300 \text{ pc}$, $\dot{E} = 6.9 \times 10^{36} \text{ erg s}^{-1}$) and PSR B1706–44 ($d \sim 3 \text{ kpc}$, $\dot{E} = 3.4 \times 10^{36} \text{ erg s}^{-1}$) which have 1sr efficiencies of $\eta = 6.6 \times 10^{-4}$ and 1.8×10^{-2} , respectively, for the same energy range and assumed spectral index. If the efficiency matches that of PSR B1706–44 with nearly identical spin properties, we infer a distance of $\sim 4 \text{ kpc}$. At the very low efficiency

inferred for the Vela pulsar, the source would need to be at a rather implausible 800 pc.

We can also use trends in the X-ray luminosities of other pulsars and PWNe to obtain rough distance estimates. For 6 other Vela-like pulsars Kargaltsev et al. (2007) find an efficiency for conversion of spindown power ranging from $\eta_X \sim 3 \times 10^{-5}$ to 3×10^{-4} in the 0.5-8 keV band. Some of this spread likely stems from variation in the ambient medium as well as differing pulsar properties. If we adopt only the unabsorbed flux of the equatorial PWN and the jets, we see that the observed $5 \times 10^{-13} \text{ergs cm}^{-2} \text{s}^{-1}$ implies a distance range of 1.3-4.1 kpc. Inclusion of emission from the extended outer nebula does not seem consistent with the flux estimates for other PWNe, but would shrink the implied distance range to 0.7-2.3 kpc. The non-thermal luminosity of the point source should also scale with spin-down power; Kargaltsev et al. (2007) note that these quantities correlate surprisingly well, with $L_{PWN} \approx 5L_{psr}^{nonth}$. For J2021, the power law flux is relatively poorly determined, but at only $0.5 \times 10^{-13} \text{ergs cm}^{-2} \text{s}^{-1}$ even the equatorial nebula represents $\sim 8\times$ this component, making it easiest to interpret the equatorial nebula as the full PWN flux and supporting the 1.3-4.1 kpc distance. We caution that this estimate should not be taken too seriously given the large scatter in efficiency ratios.

A final spectral estimate of the distance comes from the neutron star thermal flux, which if interpreted as magnetic H atmosphere emission from the full surface of a canonical neutron star, implies $d \sim 2.1R_{10}\text{kpc}$, for a 10 km local neutron star radius. If the surface spectrum is a blackbody plus power law, then larger distances (4-8 kpc) are nominally allowed. However the required $\sim 2\text{MK}$ temperature would be anomalously high for full surface emission of a Vela-aged pulsar. A polar cap could be this hot, but an implausibly small $\sim 0.8\text{kpc}$ distance would be required to match the flux to the canonical polar cap area. In sum, though, the spectrum and flux estimates for the X-ray emission from this pulsar and it's PWN, along with the comparison of the inferred γ -ray efficiency with other Vela-like pulsars implies a distance of 3-4 kpc, substantially smaller than the DM-inferred distance. We adopt an estimate of $d = 4d_4\text{kpc}$, with $d_4 \approx 1$ in what follows. The source of the extra dispersion and scattering along the line-of-sight to J2021 is yet to be identified.

3.2. Birthsite and Environment

Most pulsars show bow shock PWNe when traveling at supersonic speeds through the interstellar medium. However, with a characteristic age $\tau_c = 1.7 \times 10^4 \text{yr}$, J2021 should still reside in its parent supernova remnant, where in the absence of a central pulsar or PWN the reverse shock reaches the center on a timescale of

$$t_{Sed} \approx 7(M_{ej}/10M_{\odot})^{5/6}(E_{SN}/10^{51}\text{ergs})^{-1/2}(n_{ISM}/1\text{cm}^{-3})^{-1/3}\text{kyr} \quad (1)$$

(Reynolds & Chevalier 1984). In the presence of a young pulsar, the reverse shock will collide with the expanding PWN in a time somewhat less than this. If the remnant is just entering the Sedov phase the reverse shock should be reaching the remnant center, where it would crush the PWN. For typical high pulsar velocities the system can be well off-center in the parent SNR; the crushed PWN should then trail back toward the supernova site, with the pulsar at the leading edge (van der Swaluw, Downes & Keegan 2004). Instead, we see symmetric equatorial structure, with jets extending to $\sim 30''$ and no prominent bow shock on smaller scales. This suggests a low velocity pulsar in a relatively quiescent surrounding medium. It is possible that the reverse shock has not yet reached the PWN or, alternatively, that the reverse shock reverberations settled down some time ago, leaving a relatively uniform high-pressure SNR interior as the ambient environment. Given the characteristic age of the pulsar (17 kyr), and the timescale for the SNR reverse shock to reach the PWN (~ 5 kyr), we favor the latter interpretation.

If a $10^{51} E_{51}$ erg supernova has produced a Sedov-phase remnant of age $10^4 t_4$ y in an external medium of density $n_{ISM} \text{ cm}^{-3}$, then we expect a shell of radius

$$\theta_{\text{SNR}} \approx 12' (E_{51}/n_{ISM})^{1/5} t_4^{2/5} / d_4. \quad (2)$$

While there is no cataloged remnant and no obvious X-ray or radio shell in the vicinity, we could plausibly associate the thin arc with a partial SNR shell. However, with a radius of curvature $\sim 7'$ centered $\sim 8'$ northeast of the pulsar, it seems unlikely that this represents the limb of the parent SNR. Of course, the scale would be acceptable for the large ~ 10 kpc distance, but then the pulsar would have left the shell at $2300 d_{10}/t_4 \text{ km s}^{-1}$; the PWN should then show a bow shock with an unresolved stand-off. It is possible that the arc is a filament on the face of a larger remnant, with the pulsar close to the center. A search for a large $\sim 30'$ low surface brightness shell could be productive.

Assuming for the moment that the PWN does live in the heated interior of a Sedov-phase SNR, we expect an ambient pressure $P_{\text{SNR}} \propto \rho \dot{R}^2 = \chi \rho_{ISM}^{3/5} E_{SN}^{2/5} t^{-6/5}$. We take $\chi = 0.047$ (van der Swaluw et al. 2000) so that

$$P_{\text{SNR}} \approx 1 \times 10^{-9} E_{51}^{2/5} n_{ISM}^{3/5} t_4^{-6/5} \text{ g cm}^{-1} \text{ s}^{-2} \quad (3)$$

The PWN equatorial torus represents the termination shock where the pulsar wind momentum flux balances this pressure. Two factors complicate our estimation of the termination shock radius for J2021. First the wind is expected to be equatorially confined so that the momentum balance condition is

$$P_{\text{SNR}} \approx \dot{E} \xi / (4\pi R_{WS}^2 c) \quad (4)$$

with $\xi > 1$. For example, for a wind momentum scaling with latitude θ as $\sin^2\theta$ (Bogovalov & Khangoulyan 2002) one expects $\xi = 3/2$. Second, while in some PWNe such as the Crab, we observe the ‘sub-luminous zone’ of unshocked pulsar wind and hence directly resolve R_{WS} , here we only see the overall extent of the equatorial flow, which is generally $2\text{--}3\times$ larger (e.g. Ng & Romani 2008). Accordingly, using the pressure (3) we estimate the overall angular scale of the equatorial torus as

$$\theta_{eq} \approx (2 - 3\times) 1''.6 E_{51}^{-1/5} n_{ISM}^{-3/10} t_4^{3/5} \xi^{1/2} d_4^{-1}. \quad (5)$$

Taking $E_{51} = n_{ISM} = 1$, $\xi \approx 2$ and $t_4 = 1.7$ (the spindown age) we get an overall scale of $\theta_{eq} \sim (2 - 3\times) 3.1'' d_4^{-1}$. If we identify the double ridge of the ‘wings’ of the dragonfly with this overall torus, we have a measured size of $\approx 10''$, which from (5) implies a distance of 2.5–3.7 kpc. This is in good accord with our previous estimate of 3–4 kpc.

More heuristically, we can simply scale to the observed angular radius of the overall toroidal flow for Vela ($\sim 30''$) and PSR B1706–44 ($\sim 15''$). Matching the $\sim 10''$ of the dragonfly wings suggests ~ 1 or 4.5 kpc (for Vela and B1706, respectively). Again, while not precise, the geometrical estimate of the wind shock scale suggests a distance ≤ 4 kpc.

3.3. Outer Nebula and Jets

In Figure 4, we see that the diffuse emission surrounding the equatorial PWN is brightest in a $\sim 25''$ radius halo around the pulsar, continuing to the ‘outer nebula’ which forms a $\sim 50''$ radius limb-brightened structure surrounding the pulsar and trailing off to the west, with some curvature. If we interpret this outer nebula as a bow shock, then with a PWN speed of $10v_6 \text{ km s}^{-1}$ ($v = v_6 \times 10^6 \text{ cm s}^{-1}$) relative to an ambient medium of number density n , we have

$$\theta_{BS} \approx [\dot{E}/(4\pi c \rho v_{PSR}^2 d^2)]^{1/2} \approx 40'' n^{-1/2} / (v_6 d_4) \quad (6)$$

and the observed $\theta_{bs} \sim 50''$ standoff distance implies a rather low speed of $v_{PSR} \approx 8 n^{-1/2} d_4^{-1} \text{ km s}^{-1}$. This nebula seems to extend $\sim 4'$ to the west. If this traces the actual motion since pulsar birth we require a fairly typical pulsar speed of $v = 4'd/\tau_c = 270 d_4 \text{ km s}^{-1}$ assuming the true age is the spindown age. To preserve the large nebula standoff, the ambient medium should then have a density $n < 10^{-3} \text{ cm}^{-3}$, which is plausible for the hot interior of a SNR. Some support for this interpretation comes from the softening of the X-ray spectrum in the western half of the nebula, which could be attributed to synchrotron cooling of relic particles at the pulsar birth site. Alternatively, this outer nebula could be caused by PWNe electrons filling a pre-existing structure in the SNR interior, e.g. density variations in a progenitor wind, so it might not trace the pulsar motion.

Turning to the jet components, it is natural to attribute the flux ratio between the jet and counter jet to Doppler boosting. For a continuous co-linear inner jet/counter-jet we expect $I_j/I_{cj} = [(1 - \beta \cos \zeta)/(1 + \beta \cos \zeta)]^{-\Gamma-1}$, where ζ is the inclination of the jet axis to the line of sight. The spectral fits give $\Gamma \approx 1.1$ and a flux ratio of $1.7^{+0.8}_{-0.5}$. However, the spatial fit to the equatorial structure places it nearly edge-on ($\zeta \approx 85^\circ$), which gives a maximum flux ratio of ~ 1.4 for large β . Of course even a small jet misalignment relaxes this stricture; for $\zeta \approx 80^\circ$, we can accommodate a flux ratio of 1.7 with $\beta = 0.7$. Still, with the jets nearly in the plane of the sky large β are required for significant Doppler boosting.

A similar argument applies to the outer jets. For the jet an aperture that avoids the bright knot at the end provides 73 ± 16 counts, while the same size aperture for the counter-jet has 28 ± 14 counts (not a significant detection). This leads to a fairly large flux ratio of $2.6^{+3.8}_{-0.9}$. Of course this cannot be accommodated for an inclination as large as 85° . However, visually the jet and counter-jet do appear to be mis-aligned on the plane of the sky, so a larger counter-jet inclination, allowing larger Doppler de-boosting, does seem plausible. For example, for the observed jet spectrum ($\Gamma \approx 1.7$) any angle $< 75^\circ$ can be accommodated for $\beta < 0.7$.

In view of the possible jet variability noted above, none of these flux ratio constraints should be taken too seriously. However, if we do attribute the faintness of the outer counter-jet to Doppler boosting, then the presence of a terminal knot for both the jet and counter-jet could be due to a termination shock, resulting in slower flow with more isotropic emission. The outer nebula is somewhat brighter in a $\sim 25''$ region around the PWN and perhaps this marks the flow boundary where the jets terminate. This would be reasonable if they lie close to the plane of the sky. In any case the termination probably lies well within the envelope of the ‘outer nebula,’ with the jets only half the length of the outer nebula radius, an implausibly small inclination of 30° would be required to make their projected length as small as observed.

3.4. Energetics and Spectral Results

The observed spectral softening from the inner to the outer nebula (Figure 5) suggests aging of the synchrotron population on the flow time. At radio frequencies, however, the dominant population should be uncooled with a spectral index $\alpha_R \approx 0.3$. An examination of the 1.4GHz DRAO Galactic Plane Survey continuum maps (English et al. 1998) shows a 3 ± 0.5 mJy source at the position of J2021, not clearly resolved at the \sim arcmin GPS resolution. Since the pulsar itself provides only 0.1 mJy at 1.4GHz, we interpret this as PWN emission.

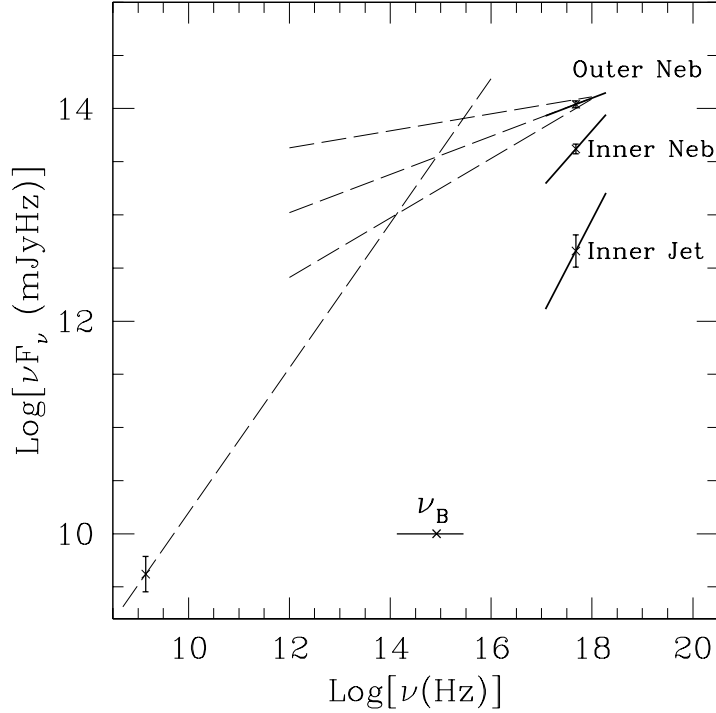


Fig. 5.— PWN synchrotron cooling. Here we show the radial softening of the PWN X-ray spectrum (see Table 2). For the dominant flux of the outer nebula we extrapolate to the observed radio flux with a $\Delta\alpha=0.5$ cooling break.

For such a low radio flux, the cooling break must be at relatively high frequency. Extrapolation of the X-ray flux with a $\Delta\alpha = 0.5$ break implies $\text{Log}[\nu_B \text{ (Hz)}] = 14.9^{+0.5}_{-0.8}$. The synchrotron break frequency at an age of $10^4 t_4 \text{ yr}$ in a field of $B_{mG} \text{ mG}$ is $\nu_B = 1.0 \times 10^{10} B_{mG}^{-3} t_4^{-2} \text{ Hz}$. Thus we infer an outer nebula field of $B = 13^{+13}_{-4} \mu\text{G}$ for $t_4 = 1.7$. This can be compared with the field extrapolated from $B_s = 3.2 \times 10^{12} \text{ G}$ at the pulsar surface ($R_s = 10 \text{ km}$). If the field is dipolar within the magnetosphere, followed by $\propto 1/r$ in the wind exterior to the light cylinder ($R_{LC} \equiv c/\omega$) we expect $B_{ws} \approx 4B_s R_s^3 / (R_{LC}^2 R_{ws}) = 220 \theta_5^{-1} d_4^{-1} \mu\text{G}$ in the wind termination shock at an angle of $5\theta_5''$. If the field continues to decrease as $\propto 1/r$ in the post-shock flow, then we would expect a value $\sim 20 \mu\text{G}$ at the $\sim 50''$ limb of the outer nebula. This is in reasonable accord with the photon-weighted value estimated from the (rather uncertain) spectral break. The corresponding magnetic pressure $B^2/8\pi \sim 2 \times 10^{-11} \text{ g cm}^{-2} \text{ s}^{-2}$ is somewhat lower than equipartition for a SNR interior. More detailed radio measurements, resolving the PWN and determining the radio spectral index would substantially tighten these arguments. It may also be useful to mount deep optical/IR imaging to detect the PWN flux near the cooling break.

4. Conclusions

We observed PSR J2021+3651 and its surrounding structured nebula and jets with the *CXO* ACIS. This ‘Dragonfly Nebula’ displays an axisymmetric morphology, with bright inner jets, an apparently double-ridged equatorial inner nebula, and a $\sim 30''$ long polar jet. Surrounding the central nebula is a low surface-brightness outer nebula. This structure brackets the pulsar at a radius of $\sim 50''$ and trails off to the west over $3\text{--}4'$. The overall structure is highly reminiscent of *CXO*/ACIS image of the PWN surrounding PSR B1706–44 (Romani et al. 2005), and, as for this source, is plausibly caused by a low-velocity pulsar in a relatively quiescent medium. No clear evidence of a host SNR is seen. IR data does appear to show a dust deficit associated with the trailed X-ray nebula.

Although the photon statistics are limited, double structure for the equatorial PWN is suggested by both the initial 19 ks exposure and, independently, by our new deeper image. So far Vela is the only other pulsar showing a double ridge in its PWN. Whether this represents a physical doubling of the equatorial torus or projection (caustic) effects in an optically thin, Doppler boosted pulsar wind is still unclear.

The new spectral data combined with the spatial scale of the PWN shock and its surrounding nebula do not support the ~ 12 kpc distance suggested by the large pulsar DM. The X-ray absorption, efficiency arguments, and comparison with other Vela-type PWNe, while individually inconclusive, all suggest a smaller $d \sim 3\text{--}4$ kpc. On the balance we prefer this distance scale, although we find no obvious source of ionized plasma that could explain an anomalously large DM, so this large value would remain unexplained.

This new distance estimate will likely be helpful in interpreting new γ -ray observations. At this distance, the GeV efficiency needed to produce the *EGRET* source is comparable to that for PSR B1706–44. Upcoming *AGILE*, and especially *GLAST*, observations should test this association. A high quality pulse profile will also be very useful, as the pulse shape is sensitive to the inclination angle ζ estimated here from the PWN fit. For example, in outer magnetosphere gap models (e.g. Romani & Yadigaroglu 1995), the large inclination angle of this pulsar predicts a double peaked γ -ray light curve with large phase separation. At higher TeV energies, the PWN may also be detectable, although the striking morphological similarity to the PWN of B1706–44 inspires a note of caution, since H.E.S.S. searches for B1706–44’s PWN find only upper limits of $0.01 \times \text{Crab}$ (Aharonian et al. 2005). However, it may be relevant that Milagro finds a source MGRO J2019+37 $\sim 20 \pm 25'$ west of PSR J2021+3651 (Abdo et al. 2007). Intriguingly, the offset from J2021 is along the direction of the ‘outer nebula’ trail. Since the TeV ICS emission is dominated by lower energy, and hence older, electrons than those that produce the X-ray synchrotron emission, such offsets are commonly seen for PWNe. A high quality IACT image from *VERITAS* or *MAGIC*

detecting the PWN and showing its arcminute-scale structure would be of particular interest. Conversely, strong upper limits on associated TeV emission would suggest that some common attribute makes the Compton component of the ‘Dragonfly Nebula’ and PSR B1706–44’s PWN anomalously faint.

We thank N. Bucciantini for interesting discussions of PWN structure. This work was supported in part by NASA grant NAG5-13344 and by Chandra grant GO7-8057 issued by the Chandra X-Ray Center, which is operated by the Smithsonian Astrophysical Observatory for and on behalf of the National Aeronautics Space Administration under contract NAS8-03060.

Facilities: CXO (ACIS)

REFERENCES

- Abdo, A. A., et al. 2007, ApJ, 658, L33
- Aharonian, F., et al. 2007, AA, 432, L9.
- Bucciantini, N. 2007, arXiv/0710.0397
- Bogovalov, S. V., & Khangoulyan, D. V. 2002, Astronomy Letters, 28, 373
- Cordes, J.M. & Lazio, T.J.W. 2002, astro-ph/0207156
- Del Zanna, L. at al. 2006, AA, 453, 621
- Dickey, J.M. & Lockman, F.J. 1990, ARAA, 28, 215
- Dodson, R., Legge, D., Reynolds, J. E., & McCulloch, P. M. 2003, ApJ, 596, 1137
- English, J. at al. 1998, PASA, 15, 56
- Getman, K. V., et al. 2005, ApJS, 160, 319
- Gotthelf, E.V. 2003, ApJ, 591, 361
- Hessels, J.W.T., *et al.* 2004 ApJ, 612, 389
- Kalberla, P.M.W. et al. 2005, A&A, 440, 775
- Kargaltsev, O., Pavlov, G. G., & Garmire, G. P. 2007, ApJ, 660, 1413

- Kargaltsev, O., & Pavlov, G. G. 2008, ArXiv e-prints, 801, arXiv:0801.2602
- Kennel, C. F., & Coroniti, F. V. 1984, ApJ, 283, 694
- Kenyon, S. J., & Hartmann, L. 1995, ApJS, 101, 117
- Komissarov, S. & Lyubarsky, Y. 2004, Ap&SS, 293, 107
- Mori, K. et al 2001, ASPC, 251, 576
- Ng, C.-Y., & Romani, R. W. 2004, ApJ, 601, 479
- Ng, C.-Y., & Romani, R.W. 2008, ApJ, 673, 411
- Pavlov, G. G., Zavlin, V.E., Sanwal, D., Burwitz, V., & Garmire, G.P. 2001, ApJ, 552, L129
- Pavlov, G.G., Teter, M.A., Kargaltsev, O. & Sanwal, D., 2003, ApJ, 591, 1157
- Pavlov, G. G., Kargaltsev, O., & Briskin, W. F. 2007, ArXiv e-prints, 707, arXiv:0707.3529
- Roberts, M. S. E., Romani, R. W., & Kawai, N. 2001, ApJS, 133, 451
- Roberts, M. S. E., Hessels, J. W. T., Ransom, S. M., Kaspi, V. M., Freire, P. C. C., Crawford, F., & Lorimer, D. R. 2002, ApJ, 577, L19
- Rees, M. J., & Gunn, J. E. 1974, MNRAS, 167, 1
- Reynolds, S.P., & Chevalier, R. A. 1984, ApJ, 278, 630
- Romani, R. W., & Yadigaroglu, I.-A. 1995, ApJ, 438, 314
- Romani, R. W., Ng, C.-Y., Dodson, R., & Briskin, W. 2005, ApJ, 631, 480
- Rosse 1844, Phil. Trans. R.S., 321.
- Schlegel, D. J., Finkbeiner, D. P., & Davis, M. 1998, ApJ, 500, 525
- van der Swaluw, E., Achterberg, A., Gallant, Y. A., & Tóth, G. 2000, ArXiv Astrophysics e-prints, arXiv:astro-ph/0012440
- van der Swaluw, E., Downes, T.P & Keegan, R. 2004, A&A, 420 937
- Zavlin V.E. et al., 1996, A&A 315, 141

	double tori	single torus
Ψ ($^\circ$)	$50.1 \pm 0.4 \pm 0.6$	$50.0 \pm 1.1 \pm 0.11$
ζ ($^\circ$)	$85.9 \pm 0.2 \pm 1.0$	$84.9^{+0.4}_{-0.3} \pm 0.2$
R ($''$)	$11.1 \pm 0.2 \pm 1.0$	$9.3^{+0.3}_{-0.2} \pm 1.0$
blur ($''$)	1.2 (fixed)	$2.9 \pm 0.04 \pm 0.2$
β	$0.84 \pm 0.01 \pm 0.001$	$0.78 \pm 0.01 \pm 0.03$
d ($''$)	$3.7 \pm 0.04 \pm 0.12$	-
Point Source (cts)	1240	1209
Torus (cts)	3896	4459

Table 1: Best-fit torus parameters for the double tori and single torus models, with 1σ statistical and systematic errors.

Table 2: Spectral Fits to PSR J2021+3651

Model +PL*	Power Law		abs.flux $f_{0.5-8}^\dagger$	unabs. flux $f_{0.5-8}^\dagger$	T^∞ MK	R^∞ d_{10}^\ddagger km	BB/NSA		χ^2/dof
	N_H 10^{21}cm^{-2}	Γ					abs. flux $f_{0.5-8}^\dagger$	unabs. flux $f_{0.5-8}^\dagger$	
BB	6.70*	-	-	-	$2.15^{+0.16}_{-0.15}$	$4.62^{+1.40}_{-0.87}$	0.29 ± 0.024	1.83 ± 0.15	62.7/81
NSA	6.70*	-	-	-	$0.88^{+0.57}_{-0.02}$	$13.1^{*\diamond}$	$0.28^{+0.018}_{-0.030}$	$2.95^{+0.19}_{-0.32}$	74.9/81
PL+BB	6.70*	$1.73^{+1.15}_{-1.02}$	0.33 ± 0.032	0.48 ± 0.048	$1.85^{+0.20}_{-0.24}$	$6.96^{+4.03}_{-1.66}$	0.23 ± 0.023	1.95 ± 0.19	32.6/79
PL+BB	$4.33^{+2.36}_{-1.75}$	$0.99^{+1.30}_{-1.40}$	0.32 ± 0.093	0.36 ± 0.11	$2.33^{+0.56}_{-0.53}$	$2.65^{+8.74}_{-2.53}$	0.26 ± 0.025	0.89 ± 0.085	30.1/78
PL+NSA	6.70*	$1.92^{+0.95}_{-1.81}$	0.32 ± 0.069	0.52 ± 0.11	$0.85^{+0.25}_{-0.093}$	$13.1^{*\diamond}$	$0.22^{+0.022}_{-0.024}$	$2.45^{+0.24}_{-0.27}$	32.0/79
PL+NSA	$7.19^{+1.77}_{-2.61}$	$1.70^{+0.99}_{-1.96}$	0.32 ± 0.076	0.48 ± 0.11	$0.87^{+0.72}_{-0.24}$	$13.1^{*\diamond}$	$0.24^{+0.023}_{-0.024}$	$2.85^{+0.27}_{-0.28}$	31.2/78

*held fixed

† 0.5-8 keV fluxes in units of $10^{-13}\text{erg}/\text{cm}^2/\text{s}$

‡ at a distance of 10 kpc

$^\diamond$ yields a distance of 2.1 kpc.

Table 3: Spectral Fits to Other Sources

Region	N_{H} 10^{21}cm^{-2}	Γ	abs. flux $f_{0.5-8}^{\dagger}$	unabs. flux $f_{0.5-8}^{\dagger}$	χ^2/dof	obs #
Inner Neb	6.7*	1.45 ± 0.09	3.2 ± 0.14	4.2 ± 0.19	84.8/200	0,1,2
Inner Jet	6.7*	$1.09^{+0.35}_{-0.34}$	0.38 ± 0.06	0.46 ± 0.07	17.0/31	0,1,2
Inner Co-Jet	6.7*	1.01 ± 0.58	0.23 ± 0.05	0.27 ± 0.06	10.7/19	0,1,2
Jet	6.7*	$1.68^{+0.47}_{-0.44}$	0.16 ± 0.03	0.23 ± 0.05	9.1/13	1,2
Outer Neb	6.7*	1.82 ± 0.10	7.2 ± 0.29	10.9 ± 0.45	417.9/655	1,2
Outer Neb - East	6.7*	1.69 ± 0.13	3.9 ± 0.23	5.7 ± 0.33	207.7/400	1,2
Outer Neb - West	6.7*	1.93 ± 0.13	3.1 ± 0.18	5.0 ± 0.28	300.1/477	1,2
Arc	6.7*	$1.66^{+0.25}_{-0.24}$	0.96 ± 0.12	1.4 ± 0.17	80.4/151	1,2
Arc	$8.8^{+5.4}_{-9.9}$	$1.87^{+0.59}_{-0.48}$	0.92 ± 0.11	1.5 ± 0.18	79.8/150	1,2
AGN	25^{+28}_{-14}	$1.84^{+1.43}_{-1.24}$	0.44 ± 0.07	0.94 ± 0.15	9.4/17	1,2
AGN	22^{+10}_{-8}	1.7*	0.45 ± 0.07	0.85 ± 0.14	9.5/18	1,2
Star	$0.20^{+0.10}_{-0.20}$	$3.45^{+0.62}_{-0.47}/16.1^{+5.8}_{-1.5}^{\ddagger}$	1.34 ± 0.17	1.43 ± 0.19	37.1/51	0
Star	$0.20^{+0.10}_{-0.20}$	$3.81^{+0.58}_{-0.36}/15.8^{+4.5}_{-1.2}^{\ddagger}$	1.23 ± 0.13	1.31 ± 0.14	57.2/68	1
Star	$0.20^{+0.10}_{-0.20}$	$2.80^{+0.43}_{-0.40}/10.1^{+1.9}_{-0.82}^{\ddagger}$	0.70 ± 0.08	0.76 ± 0.08	57.3/63	2

*held fixed

\ddagger T(MK) for two Mekal thermal components

\dagger 0.5-8 keV fluxes in units of $10^{-13}\text{erg cm}^{-2} \text{s}^{-1}$